ACS APPLIED MATERIALS & INTERFACES

Research Article

www.acsami.org

pH-Responsive Iron Manganese Silicate Nanoparticles as T_1-T_2* Dual-Modal Imaging Probes for Tumor Diagnosis

Jian Chen,[†] Wei-Jie Zhang,[∥] Zhen Guo,*[,‡] Hai-Bao Wang,*[,§] Dong-Dong Wang,[†] Jia-Jia Zhou,[‡] and Qian-Wang Chen*[,†]

[†]Hefei National Laboratory for Physical Sciences at Microscale, Collaborative Innovation Center of Suzhou Nano Science and Technology, Department of Materials Science & Engineering, CAS High Magnetic Field Laboratory, University of Science and Technology of China, Hefei 230026, China

[‡]Anhui Key Laboratory for Cellular Dynamics and Chemical Biology, School of Life Sciences, University of Science and Technology of China, Hefei 230027, China

[§]Radiology Department, First Affiliated Hospital of Anhui Medical University, Hefei 230022, China

[∥]Hefei National Laboratory for Physical Sciences at Microscale and School of Life Sciences, University of Science and Technology of China, Hefei 230027, China

Supporting Information

ABSTRACT: Magnetic resonance imaging (MRI) probes can be concentrated in tumors through grafting targeting agents. However, the clinical application of such targeted MRI probes is largely limited because specific agents are only used to target specific characteristics of cancer cells. The development of the MRI probes that can be used regardless of tumor types or their developmental stages is highly appreciated. The acidic tumor microenvironments and acidic organelles (endosomes/lysosomes) in cancer cells are universal phenomena of solid tumors, and nanoparticles can also accumulate in tumor tissues by enhanced permeability and retention (EPR) effect. Here, we reported the synthesis of pH-responsive T_1-T_2* dual-modal contrast agents based on iron manganese silicate ($FeMn(SiO_4)$) hollow nanospheres, which can release Mn^{2+} ions in acidic environments, exhibiting excellent ability as agents for magnetic resonance and red fluorescence imaging. MRI for mouse models revealed that the nanoprobes could accumulate in tumors via EPR effect and then distinguish tumors from normal tissues with the synergistic effect of T_1 and T_2* signal only 10 min after intravenous injection. Fluorescence imaging demonstrated that the nanoprobes could be endocytosed into cancer cells and located at their lower pH compartments. Moreover, the hollow nanospheres showed no obvious toxicity and inflammation to the major organs of mice, which made them attractive diagnostic agents for different types of cancers.

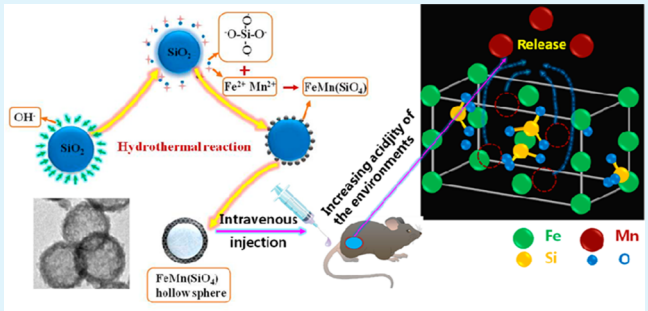

KEYWORDS: *iron manganese silicates, T_1-T_2* weighted image, fluorescence image, pH-responsive, EPR*

INTRODUCTION

Molecular imaging for cancer diagnosis and therapy has received great interest in recent years.[1−3] Magnetic resonance imaging (MRI) is one of the most useful diagnostic modalities because it can noninvasively acquire three-dimensional tomographic information for whole tissue samples with high spatial resolution.[4] However, this imaging modality usually needs contrast agents to enhance diagnostic accuracy. Today, two forms of imaging contrast agents are used for MRI; one is a T_1 type for a positive signal and the other is a T_2 type for a negative signal. The T_1 contrast agents typically use paramagnetic coordination complexes, and the T_2 contrast agents are generally superparamagnetic nanoparticles.[5] As each type of contrast agents has its intrinsic drawbacks, exact and dependable biomedical information cannot be obtained, and clinical diagnosis may be misled only by using a single imaging modality. For example, the T_2-weighted dark signal gained with contrast agents superparamagnetic nanoparticles is often mixed with the signals from calcification, bleeding, or metal deposits, and the susceptibility artifacts can impact the background image.[6] This limitation can be remedied by combining T_1 and T_2 imaging modalities because it can give highly accurate diagnostic information benefiting from both high tissue resolution contributed by T_1 imaging and high feasibility on detecting lesions contributed by T_2 imaging.[7] Thus, the development of single contrast agents which can act as T_1-T_2 dual modal MRI probes with biocompatibility is urgently demanded.

Received: December 14, 2014
Accepted: February 16, 2015
Published: February 16, 2015

DOI: 10.1021/acsami.5b00727
ACS Appl. Mater. Interfaces 2015, 7, 5373−5383

Several T_1-T_2 dual modal contrast agents have been reported in recent years, such as the nanocomposites with a core of iron oxide particles and a shell of paramagnetic gadolinium complexes[8] or Gd_2O_3-embedded iron oxide nanoparticles.[9] As MRI signal intensity is strongly dependent on the concentration of the contrast agents, enrichment of the contrast agents in tumor tissues is really demanded to make the signal in the diseased tissues more distinct than in the background. Employing nanoparticles as contrast agents can achieve this purpose because nanoparticles less than 200 nm prefer to accumulate in the tumor tissues through the EPR effect.[10] However, such nanoparticles also have high accumulation in the reticuloendothelial system (RES), particularly the Kupffer cells in the liver.[11] This conflict may lead to misdiagnosis because the signal in tumor tissues will be confused by the signal in organs of RES. Modification with targeting ligands can help nanoparticles to avoid the uptake by RES and improve their accumulation in the specific types of tumors, increasing the diagnostic accuracy and reducing the side effects.[12] However, the clinical efficacy of the agents is unsatisfactory because the expression quantity of the tumor associated receptors is dependent on the tumor types as well as their developmental stages.[13] Thus, different targeting agents need to be developed for various types of tumors, which would lead to a higher cost and workload. On the contrary, the acidic tumor microenvironments in solid tumors and acidic organelles (endosomes/lysosomes) of cancer cells are common phenomena, having no relationship with the tumor types or their developmental stages.[14] Thus, the disturbance from RES in MRI cancer detection can be avoided based on the pH-responsive nanoprobes, which can deposit in tumor tissues via EPR effect and only work in an acidic environment. Though various pH-sensitive MRI probes have been developed, such as the pH-sensitive MnO nanoparticles or Mn^{2+} ions doped SiO_2 nanospheres.[15,16] However, such probes based on Mn ions release usually have slow Mn^{2+} ions release rate because the Mn ions are in a stable coordination environment.[16,17] This deficiency requires patients to be injected with high-dose contrast agents and wait for a longer time to guarantee a high enough concentration of Mn^{2+} ions in the tumors before diagnosis, which makes patients suffer much more harm in both physical and mental aspects. In addition, the toxicity of nanomaterials themselves[18] can also hinder their clinical applications. To develop a safe and pH-sensitive T_1-T_2 dual modal nanoprobe without targeting agents for cancer diagnosis, we must achieve three major objectives simultaneously: (1) nanomaterials should have good biocompatibility, (2) nanomaterials can accumulate in tumor tissues efficiently through the EPR effect, and (3) the imaging capability of nanomaterials must be sensitive to pH value and significant signal contrast between the tumor and normal tissues must be observed immediately.

Silicates with good biocompatibility[19] and persistent luminescence[20] have been reported for many years. In the lattice of silicate olivine, Mn^{2+} ions prefer to occupy the sites that are more ionic than other metal sites,[21,22] and can be easily released in an acidic environment. Therefore, the nanoparticles of silicate olivine are appropriate candidates to be developed as pH-sensitive imaging probes. Herein, we demonstrated a mild method for preparing iron manganese silicate $FeMn(SiO_4)$ hollow nanospheres with a pure olivine structure. The r_1 or r_2 molar relaxivity can be enhanced when Mn^{2+} ions come close to circumambient water molecules.[15,16] Mn^{2+} ions in the lattice cannot be released in the circulation system due to the neutral environments, after the nanoparticles reach an acidic tumor microenvironment, Mn^{2+} ions can be released, leading to high signal-to-noise ratio for T_1-T_2* weighted MRI. Meanwhile, the luminescent centers of Mn^{2+} ions can vary from blue to red depending on their surroundings,[23] which can assist the MRI probe for cancer diagnosis with red fluorescence at the cellular level. In addition, Fe, Mn, and Si are common trace elements in human body. Thus, $FeMn(SiO_4)$ hollow nanospheres may serve as safe pH-responsive T_1-T_2* dual-modal contrast agents for different types of cancers imaging.

EXPERIMENTAL SECTION

Materials. Tetraethyl silicate (TEOS, 98%), ammonia−water ($NH_3{\cdot}H_2O$, 28%), ferrous sulfate heptahydrate ($FeSO_4{\cdot}7H_2O$, ≥99%), manganese chloride tetrahydrate ($MnCl_2{\cdot}4H_2O$, ≥99%), ammonium chloride (NH_4Cl, ≥99.5%) were of analytic grade from the Shanghai Chemical Factory, China. All chemicals were used as received without further purification.

Synthesis of $FeMn(SiO_4)$ Hollow Nanospheres. The iron manganese silicate $FeMn(SiO_4)$ hollow nanospheres were synthesized via a facile hydrothermal method. First, the preparation of monodispersed silica colloidal spheres were realized based on the noted Stöber method with some modification.[24] Then, $FeSO_4{\cdot}7H_2O$ (0.5 mmol), $MnCl_2{\cdot}4H_2O$ (0.25 mmol) and NH_4Cl (15 mmol) were dissolved in distilled water (25 mL) followed by adding $NH_3{\cdot}H_2O$ (1 mL) at room temperature. Silica colloidal spheres were also dispersed in distilled water (25 mL) homogeneously. Under ultrasonic vibrations, the above two solutions were mixed homogeneously and then transferred into a Teflon-lined stainless-steel autoclave (50 mL) with heating to a temperature of 140 °C for 16 h. After cooling to room temperature naturally, the obtained $FeMn(SiO_4)$ hollow nanospheres were washed with distilled water and ethanol several times and then dried at 60 °C for further characterization.

Mn^{2+}/Fe^{2+} Ions Release Experiment. The release of Mn^{2+}/Fe^{2+} ions from $FeMn(SiO_4)$ hollow nanospheres were performed at 37 °C with suspensions (6 mL) containing 6 mg of the nanospheres at different pH values. Phosphate buffered saline (PBS) of pH = 7.4 (group 1), PBS of pH = 6.8 (group 2) and hydrochloric acid buffer solution of pH = 5 (group 3) were employed as release media to imitate normal blood/tissues, tumor environments and lysosomes, respectively. In each group, one sample was centrifuged to remove the nanospheres at a designated time point, such as 8, 16, or 24 h. Finally, the supernatant was withdrawn for determining the concentration of released Mn^{2+}/Fe^{2+} ions using inductively coupled plasma (ICP).

Magnetic Resonance Imaging (MRI) Measurement in Solution. Relaxation properties of $FeMn(SiO_4)$ hollow nanospheres in buffer solutions with different pH values (pH 7.4 and 5) were tested at 25 °C with using a clinical magnetic resonance (MR) scanner (GE HDxt; 3.0 T). Tubes containing different concentration of $FeMn(SiO_4)$ hollow nanospheres suspension, ranging from 0.06 to 3.00 mM for Fe ions, and 0.03 to 1.5 mM for Mn ions were placed into the MR scanner. T_1-weighted MR images were obtained by using a saturation recovery spin−echo sequence (TE = 10 ms, TR = 4000, 2000, 1000, 500, 200, and 100 ms, respectively). T_2*-weighted images were also obtained by Carr−Purcell−Meiboom−Gill method with the RARE sequence using the parameter of TR = 120 ms, TE = 2.328, 6.112, 9.896, 13.68, 17.46, and 21.24 ms, FA = 30°, bandwidth = 31.25 Hz, FOV 180 × 180 mm, slice thickness = 3 mm without gap.

Cell Culture and Viability Tests. The in vitro cytotoxicity of $FeMn(SiO_4)$ hollow nanospheres was assessed on A549 cells using the MTT method. Cells were cultured in a 96-well plate and maintained as subconfluent monolayers in Dulbecco's modified Eagle's medium (Invitrogen) with 10% fetal bovine serum (Hyclone, Logan, UT) and 100 units/mL penicillin plus 100 g/mL streptomycin (Invitrogen) at 37 °C with 8% CO_2. Then, 24 or 48 h later, the samples with different concentrations (25, 50, 100, 200 μg/mL) were added to the culture medium for another 24 h. Followed by putting MTT solution into

DOI: 10.1021/acsami.5b00727
ACS Appl. Mater. Interfaces 2015, 7, 5373−5383

each well, the cells were sequentially cultured for another 4 h. The absorbance of each well was measured with an ELISA reader.

Fluorescence Imaging and Observation of Intracellular Location of FeMn(SiO_4) Hollow Nanospheres in A549 Cells by a Confocal Microscopy. The fluorescence imaging was performed with excitation wavelengths of 488 and 543 nm to confirm that FeMn(SiO_4) hollow nanospheres display an emission in the red region (600−700 nm). A549 cells were seeded onto Lab-Tek Chambered 1.0 Borosilicate Coverglass system (Nunc) and incubated with FeMn(SiO_4) hollow nanospheres at 37 °C for 24 h under the atmosphere of 5% CO_2. After that, A549 cells were rinsed three times in PBS to remove the nanospheres that had not been taken up by the cells. Then, the cells were maintained in CO_2-independent medium (Gibco) containing 10% (v/v) fetal bovine serum (Hyclone, Logan, UT) and tested by a laser scanning microscope (Zeiss L SM 710) using a 40 × 1.3 numerical aperture PlanApo objective at 37 °C. Adobe Photoshop was used to construct figures.

Lysosomes were transfected by mcherry-LAMP-1 protein (lysosome-associated membrane protein 1, which specifically localized at the lysosome membrane). A549 cells were seeded onto Lab-Tek Chambered 1.0 Borosilicate Coverglass system (Nunc). Lipofectamine 2000 (Invitrogen life technologies) premixed with mcherry LAMP-1 were added into the culture medium when the cell density reached 50%. And the cells were incubated for another 4 h for transfection. After that, FeMn(SiO_4) hollow nanospheres were also added into the medium with incubation for another 24 h. Then, the cells were washed three times with PBS (pH = 7.4) and maintained in CO_2-independent medium (Gibco) containing 10% (v/v) fetal bovine serum (Hyclone, Logan, UT). Images were obtained at 37 °C with a laser scanning microscope (Zeiss L SM 710) using a 40 × 1.3 numerical aperture PlanApo objective. Adobe Photoshop was used to construct figures.

In Vivo MR Imaging. All the animal experiments were performed based on a protocol permitted by the Ethical Committee of the Experimental Animal Center of Medical University of Anhui, China, and the Animal Care Committee of University of Science and Technology of China. The mouse models with subcutaneous tumors were established by injecting 0.1 mL of cell suspension (including 5 × 10^6 human lung adenocarcinoma cancer cells (A549)) into female nude mice (purchased from Hunan SJA Laboratory Animal Co., Ltd., weighing 18−20 g) subcutaneously in the thigh region. About 15 days after inoculation, the mice were employed for imaging studies on a 3T MRI scanner (GE Signa HDX 3.0 T). After obtaining the preinjection T_1 and T_2* MR images, FeMn(SiO_4) hollow nanospheres were injected into the mice (4 mg of Mn and 7.8 mg Fe per kilogram of mouse body weight) via the tail vein. Then, T_1 and T_2* MR imaging was performed sequentially 10 and 30 min after the intravenous injection. A fast spin echo multislice (fSEMS) sequence was adopted and the parameters were shown as follows: T_1-weighted MRI sequence (repetition time (TR)/echo time (TE) = 780/19.6 ms, number of excitations (NEX) = 2, echo train length = 2, 0.188 × 0.188 mm in plane resolution with a slice thickness of 2 mm and 10 slices), and T_2*-weighted MRI sequence (repetition time (TR)/echo time (TE) = 3000/110 ms, number of excitations (NEX) = 2, echo train length = 2, 0.188 × 0.188 mm in plane resolution with a slice thickness of 2 mm and 10 slices).

Immunohistochemistry (IHC) Staining. FeMn(SiO_4) hollow nanospheres dispersed in 200 μL of saline were injected into female nude mice through the tail vein at a single dose of 60 mg/kg. The control group was intravenously administered with 200 μL saline. After 36 h, the experimental animals were sacrificed, and the major organs, such as liver, kidney, and lung were removed for histological confirmation. According to the standard techniques for histological examination, the obtained tissues were fixed in 10% formalin, implanted in paraffin, sliced, and stained with hematoxylin and eosin (H&E). Finally, an optical microscope was used for the observation of slides.

Characterization. The X-ray powder diffraction (XRD) patterns were collected on an X-ray diffractometer (Japan Rigaku D/MAX-cA X-ray) equipped with Cu−Kα radiation over the 2θ range of 10−70°. The composition of the products was determined by the energy-dispersive X-ray spectrum (EDS) which is the attachment of the high-resolution transmission electron microscopy (HRTEM) (JEOL-2010 transmission electron microscope). The morphology of the as-synthesized samples was observed using a transmission electron microscope (TEM, Hitachi model H-800) and a scanning electron microscope (SEM, JEOL JSM-6700M). Specific surface areas were calculated from the results of N_2 physisorption at 77 K (Micromeritics ASAP 2020) by using the Brunauer−Emmet−Teller (BET) and Barrett−Joyner−Halenda (BJH). The Fourier transform infrared spectrophotometry (FT-IR) spectrum was obtained using a Magna-IR 750 spectrometer in the range of 400−4000 cm^{-1} with a resolution of 4 cm^{-1}. The fluorescence emission spectra were recorded on a Labram-HR confocal laser micro-Raman spectrometer equipped with a 514 nm laser source. The concentration of Mn, Fe ,and Si ions was measured using inductively coupled plasma-atomic emission spectroscopy (ICP, Atomscan Advantage).

RESULTS AND DISCUSSION

Synthesis of FeMn(SiO_4) Hollow Nanospheres. Structural richness and good biocompatibility of silicates make them good candidates for biomedical applications. Meanwhile, micro/nanoscale hollow nanoparticles with a high surface area are promising to enhance the accessibility of outer medium to inner chamber and then improve the contact area. Herein, we have prepared hierarchical FeMn(SiO_4) hollow nanospheres via a modified chemical-template etching technique.[25] Figure 1 schematically illustrated the preparation process. First, silica colloidal spheres are dispersed into an alkaline solution including $MnCl_2$, $FeSO_4$, $NH_3{\cdot}H_2O$, and NH_4Cl. Because Si−O bonds can be broken by hydroxide ions at high temperatures, silicate ions are released from the silica templates accompanied by the generation of surface active sites.[26,27] Meanwhile, the deposition of iron or manganese hydrate can be prevented due to the presence of NH_4Cl in the solution. Then, the generated silicate ions react with Mn^{2+} and Fe^{2+} ions to form FeMn(SiO_4) particles. As the concentration of silicate ions around the SiO_2 nanoaprticles is higher than that in the other parts of the autoclave,[28] and active sites have been formed on the surface of SiO_2, the as-generated FeMn(SiO_4) particles prefer to deposit on the surface of SiO_2 cores. During this process, all Mn^{2+} ions and Fe^{2+} ions take part in the formation of FeMn(SiO_4) shell by reacting with the gradual released silicate ions from the SiO_2 spheres, forming the SiO_2@FeMn(SiO_4) core@shell structure. Finally, the remaining silica cores are dissolved completely in an

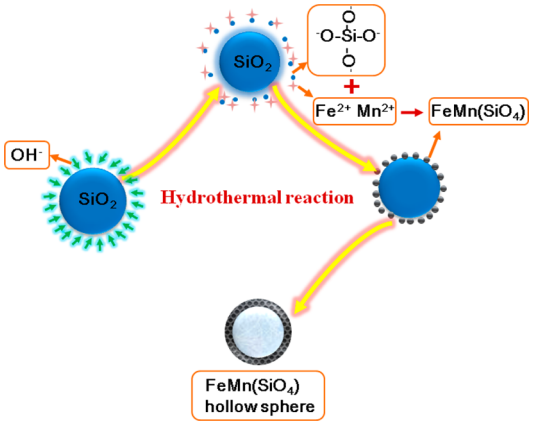

Figure 1. Schematic illustration of the preparation of FeMn(SiO_4) hollow nanospheres.

DOI: 10.1021/acsami.5b00727
ACS Appl. Mater. Interfaces 2015, 7, 5373−5383

alkaline solution at high temperatures and well-structured FeMn(SiO_4) hollow nanospheres are constructed.

The morphology of the as-synthesized products was examined by scanning electron microscopy (SEM) and transmitting electron microscopy (TEM). As shown in Figure 2a, the final products consist of sphere-like particles with

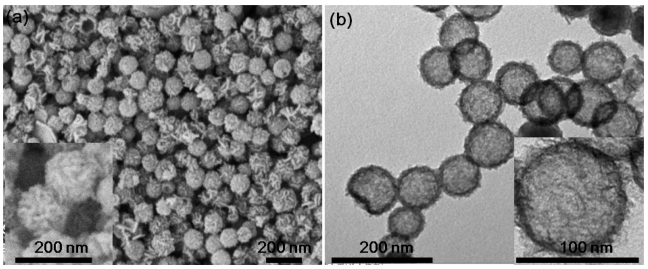

Figure 2. (a) SEM and (b) TEM images of FeMn(SiO_4) hollow nanospheres.

diameters around 80 nm. The surface of the nanospheres is rough and assembled by a great amount of nanosheets. The TEM images (Figure 2b) illustrate that the final product has a hollow structure with an obviously dark edge and pale center region. The uniform shell is about 5.5 nm in thickness.

Figure 3a shows that the diffraction pattern of the products, which can be indexed to orthorhombic iron manganese silicate with the chemical formula of FeMn(SiO_4) (JCPDS file 87-1794), belongs to the olivine structure.[29] The result also indicates that the product has a poor crystallinity, which often appears between noncovalently bound layers.[30] This conclusion is consistent with the report that in olivine structure, the bonded interactions within the layers are weakest.[22] The result of energy-dispersive spectroscopy (EDS) analysis (Figure S1, SI) confirms that the as-prepared products consist of Si, O, Mn, and Fe atoms. The inductively coupled plasma atomic emission spectroscopy (ICP-AES) analysis shows that the molar ratio of Fe, Mn, and Si in FeMn(SiO_4) hollow nanospheres is about 18:9.7:1. This data indicates that the nanospheres have the potential to be an efficient T_1-T_2* dual modal contrast agent for MRI. Figure 3b shows FTIR spectra of the template of SiO_2 nanoparticles and the obtained FeMn(SiO_4) hollow spheres. The peak at 3429 cm^{-1} indicates the residual broken bonds (Si−OH groups) on FeMn(SiO_4) hollow nanospheres. According to the above experiment results, we suggest that the crystal is held together through van der Waals forces. Thus, the as-prepared FeMn(SiO_4) hollow nanospheres are unstable, and the surface Si−OH groups will adsorb or dissociate hydrogen ions based on the pH value of the environments, inducing positive, negative, or uncharged sites.[25] This special property makes the pH-responsive release of ions possible. In addition, the surface Si−OH groups could make the nanospheres hydrophilic and weaken the clearance of them by RES, inducing the increase of their circulation time.[31] The N_2 adsorption and desorption of FeMn(SiO_4) hollow nanospheres were also measured. As shown in Figure S2 (SI), the isotherm is identified as type IV, which is characteristic of mesoporous materials. The Brunauer−Emmett−Teller (BET) surface area and total pore volume are calculated to be 221.69 m^2 g^{-1} and 0.69 cm^3 g^{-1}, respectively. The mesoporous size distribution according to the Barrett−Joyner−Halenda (BJH) method clearly exhibits that the pore size distribution is centered at 4.1 nm. The above results reveal that the product has a mesoporous structure, which would increase the contact area between the hollow nanospheres and the outer medium, making the release of Mn^{2+} ions in an acidic environments more easily.

Characterization of The pH-Responsive Magnetic Relaxation Property of FeMn(SiO_4) Hollow Nanospheres. The release of Mn^{2+} ions from FeMn(SiO_4) hollow nanospheres was measured in PBS with pH 7.4 (the pH value of body fluid), pH 6.8 (the pH value of tumor environments) and pH 5 (the pH value of the lysozome)[32] by analyzing supernatant (obtained through centrifugation at different time intervals) with ICP-AES. As shown in Figure 4, only very small

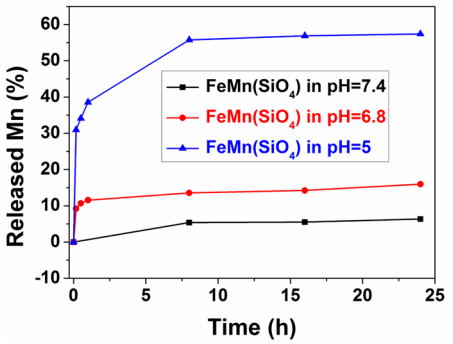

Figure 4. Release of Mn^{2+} ions from FeMn(SiO_4) hollow nanospheres in buffer solutions at pH 7.4, 6.8, and 5, respectively.

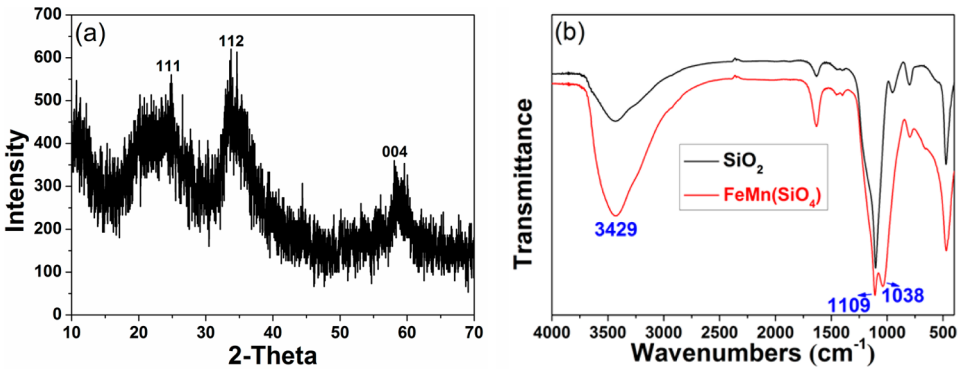

Figure 3. (a) X-ray diffraction pattern for the product of FeMn(SiO_4) hollow nanospheres; (b) FT-IR spectra of SiO_2 nanoparticles and FeMn(SiO_4) hollow nanospheres.

DOI: 10.1021/acsami.5b00727
ACS Appl. Mater. Interfaces 2015, 7, 5373−5383

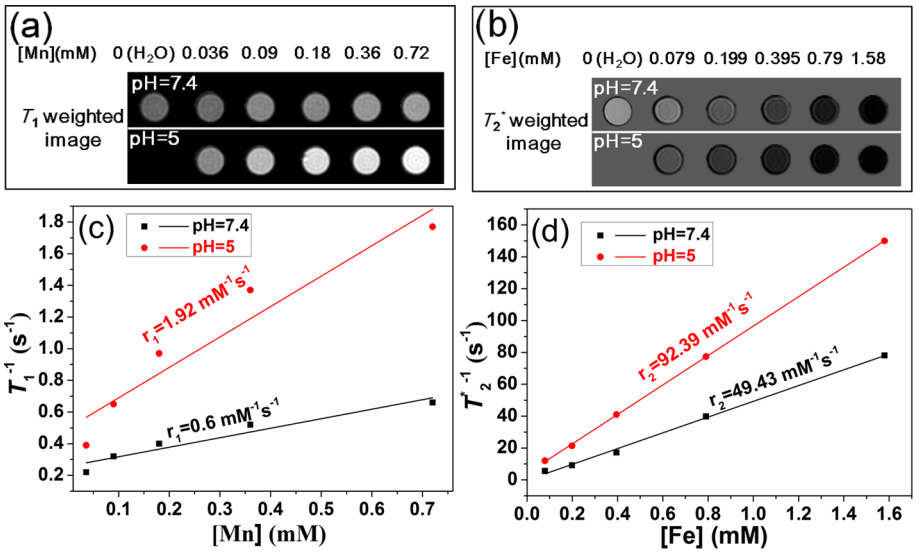

Figure 5. T_1- and T_2*-weighted MR images of $FeMn(SiO_4)$ hollow nanospheres dispersed in buffer solutions at pH (a) 7.4 and (b) 5. (c) Relaxation rate R_1 vs Mn concentration or (d) relaxation rate R_2* vs Fe concentration for nanospheres in buffer solutions at pH 7.4 and pH 5. Relaxivity values r_1 or r_2 were obtained from the slopes of linear fits of experimental data.

amount of Mn^{2+} ions has been released (6.34%) from $FeMn(SiO_4)$ hollow nanospheres at pH = 7.4 after 24 h. However, more Mn^{2+} ions would be liberated within the same interval with the pH value of the solution decreased. There are 15.97% Mn^{2+} ions released from the spheres at pH = 6.8, and at pH = 5, the released amount can even reach 57.4%. Meanwhile, the concentration of Fe^{2+} ions was also measured using ICP-AES. Interestingly, the Fe^{2+} ions release behavior was totally different from that of Mn^{2+} ions. Negligible Fe^{2+} ions were leaked out either in a neutral solution or acidic solution after 24 h. This phenomenon may be related to the crystal structure of olivine, which was described as a distorted hexagonal close packed array. In such a structure, O atoms with divalent metal (M) atoms tucked away one-half of the available octahedral voids, and one-eighth of the available tetrahedral voids were occupied by Si atoms. That is, every O atom is bonded to three M atoms and one Si atom.[33] Considering a refinement of the O, M, and Si atomic scattering factors, the M atoms were found to occupy two M sites (M1, M2). And M atoms at the M(2) sites were considered to be more ionic than those at M(1) sites.[22] According to the results mentioned above, it is suggested that in the lattice of $FeMn(SiO_4)$ (Figure S3, SI), Fe atoms occupy the M(1) sites, while Mn atoms occupy the M(2) sites.[21] Thus, Mn atoms in $FeMn(SiO_4)$ hollow nanospheres are more active than Fe atoms and can be released in an acidic environment more easily.

The magnetic properties are crucial for the successful performances of magnetic nanoparticles in MRI,[34] the magnetism of $FeMn(SiO_4)$ hollow nanospheres was measured using a SQUID device at 300 K (Figure S4, SI). The Ms value of $FeMn(SiO_4)$ hollow spheres is 0.95 emu/g, which is much lower than that of the prevailing T_2 contrast agents based on superparamagnetic iron oxide nanoparticles. Though the low Ms goes against the T_2*-weighted image contrast,[35] it can avoid generating an induced magnetic field by an external magnetic field, which may lead to an undesirable decrease of T_1 signal[36] and fluorescence quenching.[37] As Mn^{2+} ions have the ability to enhance both T_1 and T_2 relaxations,[16] we suggested that in an acidic environment, the low Ms was favorable for the enhancement of T_1 signal intensity generated from the released Mn^{2+} ions. Meanwhile, the Mn^{2+} ions could increase the T_2 signal intensity, therefore, remedying the weak T_2-weighted image contrast effect due to the low Ms.

To further explore how the pH value modulates the MRI contrast performance of $FeMn(SiO_4)$ hollow nanospheres, we investigated the capability of $FeMn(SiO_4)$ hollow nanospheres as T_1-T_2* dual modal contrast agents in PBS with pH 7.4 and 5, respectively. It can be observed that in a neutral solution, $FeMn(SiO_4)$ hollow nanospheres have no obvious effect on T_1-weighted MRI. However, when the nanospheres are dispersed in a buffer solution with pH 5, T_1 contrast effect will become more and more obvious with the increasing of nanospheres concentration. Meanwhile, T_2* images in the acidic solution become much darker compared with that in the neutral solution at the same concentration (Figure 5a,b). These results indicate that $FeMn(SiO_4)$ hollow nanospheres can act as both negative and positive contrast agents responsive to pH value, which is also consistent with the specific relaxivities of $FeMn(SiO_4)$ hollow nanospheres, r_1 and r_2, calculated by measuring the relaxation rates as a function of the concentration of Mn or Fe. The r_1 and r_2 values of the hollow nanospheres in a neutral solution are found to be 0.6 mM^{-1} s^{-1} and 49.43 mM^{-1} s^{-1}, respectively. However, the corresponding values obtained from the buffer solution with pH 5 are increased to 1.92 and 92.39 mM^{-1} s^{-1}, respectively (Figure 5c,d). All the above results suggest that the performance of $FeMn(SiO_4)$ hollow nanospheres as MRI contrast agents can be greatly affected by pH value.

Combined with the fact that T_1 contrast can be enhanced when a lot of high-spin metal ions are distributed on the surface of nanoparticles for interacting with the surrounding water molecules,[38] the pH-responsive activation of T_1 contrast-improved performance was explained as follows. The Mn^{2+} ions were located in octahedral lattice sites of $FeMn(SiO_4)$ and could not contact with the water molecules at neutral pH, inducing the low relaxivity values and negligible signal enhancement in MRI. However, Mn^{2+} ions could be released when $FeMn(SiO_4)$ hollow nanospheres were exposed in an acidic buffer solution due to the weak metal-O bonded interactions in olivine,[22,30] the mesoporous structures, and

DOI: 10.1021/acsami.5b00727
ACS Appl. Mater. Interfaces 2015, 7, 5373−5383

poor crystallinity. Then, the free Mn^{2+} ions could interact with the surrounding water molecules, resulting in the increase of MRI contrast. Besides, the profile of Mn^{2+} ions release (Figure 4) also shows that $FeMn(SiO_4)$ hollow nanospheres have a 30.95% Mn^{2+} ions release even after 10 min in a buffer solution with pH 5, which indicates that the hollow nanospheres are sensitive to the acidic environment and have a burst Mn^{2+} ions leaking within a few minutes. Several smart contrast agents which are sensitive to pH value and exhibit high r_1 values have been reported, however, they have lower Mn^{2+} ions release rates. The amount of the released ions after 48 h is even lower than that from $FeMn(SiO_4)$ hollow nanospheres within only 1 h.[16,17] The fast release rate guarantees the MRI signal being increased immediately once the contrast agents reach the tumors, and avoids the contrast agents being metabolized and excreted before liberating enough ions for the enhancement of MRI signal.

Given that few Fe^{2+} ions can be liberated from $FeMn(SiO_4)$ hollow nanospheres, we believed that the enhancement of T_2* relaxation was not attributed to the free Fe^{2+} ions. It has even been reported that Fe^{2+} ions can shorten the transverse relaxation time.[39] To explore whether the T_2* signal intensity was enhanced by the released Mn^{2+} ions, we dispersed $FeMn(SiO_4)$ hollow nanospheres in a buffer solution of pH 5, washed them several times, and redispersed them in the neutral aqueous solution (the molar ratio of Fe and Mn was changed from 1.83:1 to 5.88:1) for MRI. Figure 6 shows that

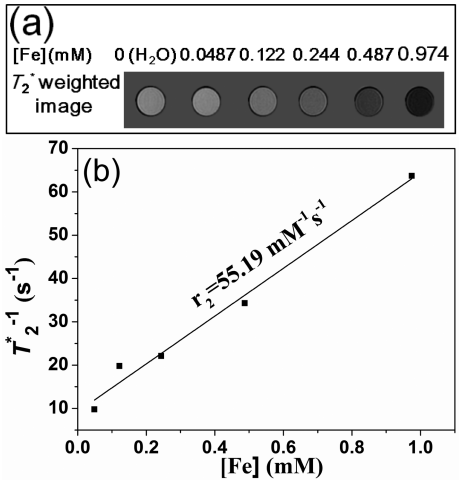

Figure 6. (a) T_2*-weighted MR images of $FeMn(SiO_4)$ hollow nanospheres with Mn^{2+} ions removed. (b) Relaxation rate R_2* vs Fe concentration for nanospheres with Mn^{2+} ions removed. Relaxivity values r_2 were obtained from the slopes of linear fits of experimental data.

the r_2 value of $FeMn(SiO_4)$ hollow spheres decreases to 55.19 mM^{-1} s^{-1} due to the lose of Mn^{2+} ions, which indicates that the increase of the T_2* signal intensity in an acidic solution is associated with the released Mn^{2+} ions. Meanwhile, we suggested that the Fe atoms in the hollow spheres also make a contribution to T_2* relaxation because the r_2 value obtained here is close to that measured in the solution with pH = 7.4. Thus, the T_2* relaxation in the neutral solution mainly originated from the intrinsic magnetism of the materials. Once the hollow nanospheres were dispersed in an acidic environment, the released Mn^{2+} ions also played a significant role, making the T_2* signal intensity high enough for imaging in vivo.

To evaluate the performance of Mn^{2+} ions released from $FeMn(SiO_4)$ hollow nanospheres for imaging tumors, we performed in vivo MRI experiments. The mouse tumor models were established by implanting A549 cells in proximal thigh region. T_1- and T_2*-weighted MR images (Figure 7a) were

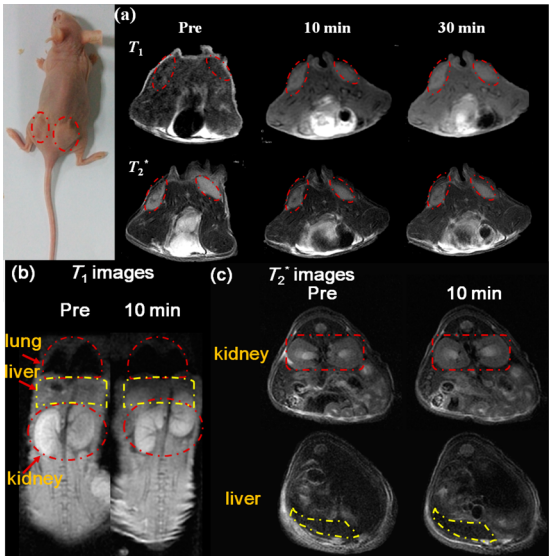

Figure 7. (a, top) T_1- and (bottom) T_2*-weighted in vivo MR images of tumors before and 10 and 30 min after intravenous injection of $FeMn(SiO_4)$ hollow nanospheres; (b) T_1-weighted in vivo MR images (coronal planes) of (top) lung circled with dashed line, (middle) liver circled with dashed line, and (bottom) kidney circled with dashed line before and 10 min after intravenous injection of $FeMn(SiO_4)$ hollow nanospheres; (c) T_2*-weighted in vivo MR images (transverse planes) of (top) kidney circled with dashed line and (bottom) liver circled with dashed line before and 10 min after intravenous injection of $FeMn(SiO_4)$ hollow nanospheres.

serially acquired before and after the injection of $FeMn(SiO_4)$ hollow spheres (4 mg of Mn and 7.8 mg of Fe per kg of mouse body weight) via the tail vein. T_1-weighted MR images show that contrast enhancement can be observed in both the periphery and the tumor interior even at the 10 min time point postadministration. The responsive time for T_1 contrast enhancement is shorter than that of the other smart contrast agents relied on pH which start to appear signal enhancement 3 h after uptake.[17] This result is related to the Mn^{2+} ions release rate. As mentioned above, the special crystal structure of $FeMn(SiO_4)$ facilitates a faster release rate for Mn^{2+} ions, leading to the immediate responsive time to enhance the MRI signal, which is important for $FeMn(SiO_4)$ hollow nanospheres to carry out their in vivo function before the released Mn^{2+} ions are renally cleared. On the contrary, a lower release rate of Mn^{2+} ions goes against the clinical application of the contrast agents. As enough high concentration of Mn^{2+} ions is required to cause significant contrast for MRI, by using contrast agents with a low Mn^{2+} ion release rate, patients need to be injected with a higher dose of contrast agents and wait for a longer time for a sufficient amount of Mn^{2+} ions to accumulate in the tumors before diagnosis. These drawbacks make patients suffer much more harm in both physical and mental aspects. In addition, 30 min after the injection of contrast agents, the T_1 signal changed slightly, which is consistent with the release

DOI: 10.1021/acsami.5b00727
ACS Appl. Mater. Interfaces 2015, 7, 5373−5383

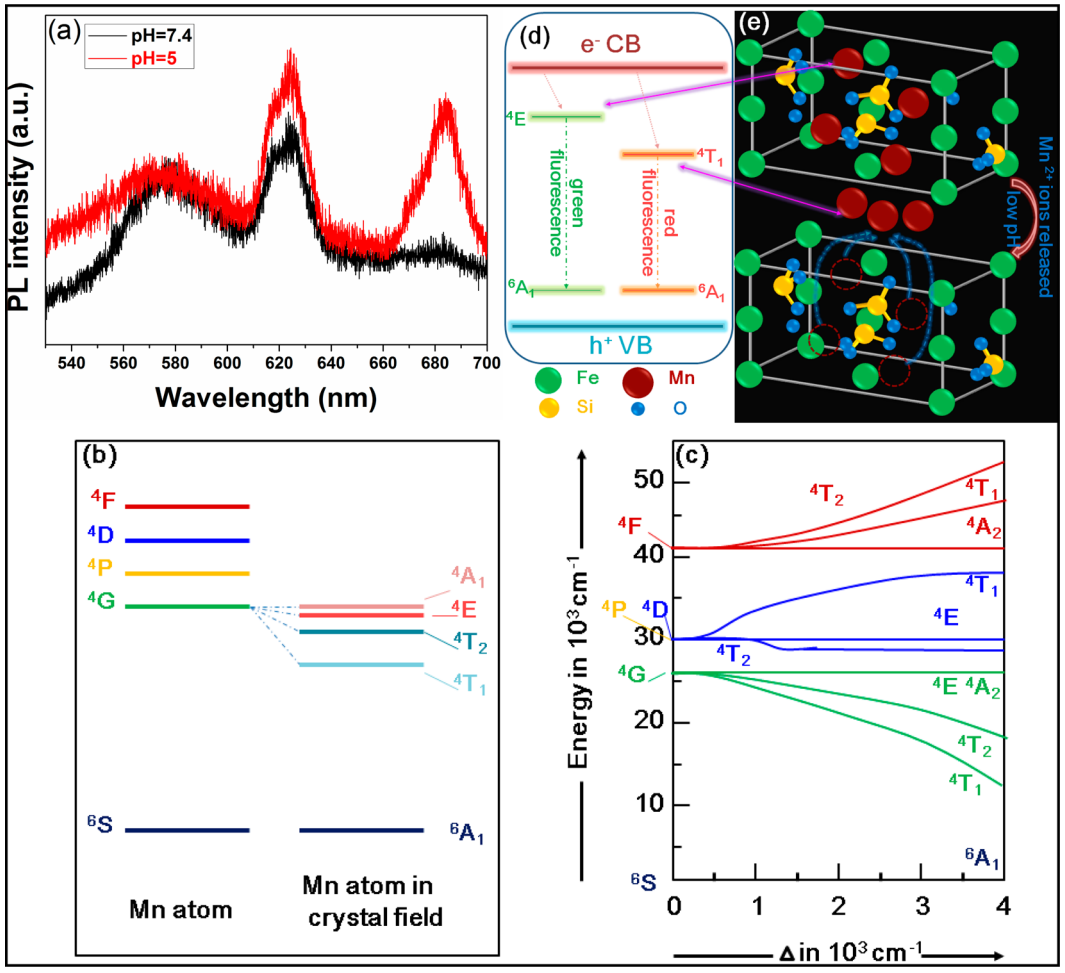

Figure 8. (a) Emission spectra of $FeMn(SiO_4)$ hollow nanospheres dispersed in different buffer solution with pH 7.4 and pH 5. (b) Schematic energy level diagram of Mn in the $FeMn(SiO_4)$ lattice; (c) Simplified Tanabe-Sugano diagram for Mn^{2+} (d^5 electronic configuration in octahedral coordination);[53] (d) Proposed energy transfer mechanisms under the excitation of 514 nm laser. (e) Schematic representations for the changing of $FeMn(SiO_4)$ structure at different buffer solution with forming Mn^{2+} cation vacancies.

result that a burst of Mn^{2+} ions leaked within a few minutes and then the ions release rate declined. Meanwhile, T_2*-weighted MR images also exhibit a clearer outline of tumors and darker signal in the interiors 10 min after injecting $FeMn(SiO_4)$ hollow nanospheres. However, the contribution of the further released Mn^{2+} ions to T_2* signal enhancement is not observed. This may be caused by the small amount of Mn^{2+} ions released during time intervals of 10−30 min. Even so, the enhanced T_2* contrast effect can be achieved with the aid of the released Mn^{2+} ions during the first 10 min.

Meanwhile, the organs lung, liver and kidney have also been tested with MR imaging before and after injecting the contrast agents intravenously. T_1-weighted images at coronal planes (Figure 7b) show that the outline of kidney becomes more clear 10 min after the intravenous injection of contrast agents. According to the current reports, Mn^{2+} can be eliminated through renal clearance,[40] while nanoparticles with diameter larger than 6 nm cannot be excreted by kidneys.[41] Thus, the basal signal increase in kidney can be attributed to the detached Mn^{2+} ions which may be liberated from $FeMn(SiO_4)$ hollow nanospheres in tumors and then enter into kidney via blood circulation and metabolism. Although the released Mn^{2+} ions can be taken up by kidney, many of them are still retained in acidic tumors within the 10 min. Thus, the T_1-weighted imaging signal in tumors is still more obvious than that in kidneys. Meanwhile, this conclusion can be further confirmed by transverse T_2*-weighted images. As shown in Figure 7c, the change of T_2* signal in kidney is also less obvious than that in tumors 10 min after injecting the contrast agents, which indicates that the amount of Mn^{2+} ions accumulated in kidneys is small. In addition, T_1-weighted images of lung and liver (Figure 7b) exhibit no significant brighter signal at the 10 min time point postadministration. Given that nanoparticles without targeting agents are ended up in RES, especially taken up by the liver,[11] $FeMn(SiO_4)$ hollow nanospheres should be mainly metabolized in liver finally. Because the modulation of T_1-weighted imaging by $FeMn(SiO_4)$ hollow nanospheres is extremely depended on pH value, the unconspicuous variation of T_1 imaging in liver indicates that there is few Mn^{2+} ions released from $FeMn(SiO_4)$ hollow nanospheres in the neutral environments of liver. Because $FeMn(SiO_4)$ hollow nanospheres themselves have the ability to act as T_2* imaging contrast agents, the T_2*-weighted images of liver were taken to further explore the biodistribution information. Figure 7c displays that the signal in liver becomes a little darker 10 min after the intravenous injection of contrast agents. This result confirms that $FeMn(SiO_4)$ hollow nanospheres are really concentrated in liver. However, the small signal change is

DOI: 10.1021/acsami.5b00727
ACS Appl. Mater. Interfaces 2015, 7, 5373−5383

related to a small number of FeMn(SiO_4) hollow nanospheres accumulated in the liver, which indicates the nanospheres have a long circulation time in blood.

T_1- and T_2*-weighted MR images of subcutaneous cancer models in mice could be acquired after intravenous injection of FeMn(SiO_4) hollow nanospheres. The nanospheres could reach the tumor tissues through EPR effect and even enter into the acid organelles of endosomes and lysozomes through endocytosis. With the migration of the nanpospheres into acidic environments, a large number of Mn^{2+} ions could be liberated rapidly, leading to the enhancement of MRI signal intensity. The improved negative contrast between tumors and surroundings from T_2*-weighted MR images indicated the occurrence of lesions. However, because the signal from the liver also became darker, the accuracy of diagnosis could not be achieved unilaterally and hastily. These drawbacks could be remedied by T_1 imaging due to pH-responsive ability of the contrast agents. The T_1-weighted MR images showed a brighter signal in the tumors, while no brighter signal can be found in the liver, further confirming the existence and location of the lesions.

Though various MRI nanoprobes with high effectiveness for in vivo imaging have been reported, enrichment of the nanoprobes in solid tumors is usually needed by EPR effect or targeting modification,[8,9] which have limitations in clinical applications. For instance, as nanoparticles that can be taken up by tumors through EPR effect can also accumulate in RES, the diagnostic information for tumors obtained by concentrating nanoprobes in tumors via EPR effect may be disturbed by the signals from RES organs. In addition, because different tumor types have various tumor-associated receptors with different expression quantity, it is a huge and complicated project to develop appropriate targeting agents for different types of tumors and conjugate them to a certain probe. Thus, the wide application of these probes for tumor diagnosis in clinic is unavailable. However, FeMn(SiO_4) hollow nanospheres can accumulate in tumors through EPR effect and distinguish the tumors from the normal tissues easily by their sensitivity to tumor acidic microenvironments and T_1-T_2* dual modal imaging ability. Such MRI contrast agents can largely improve the accuracy of cancer diagnosis and expand the range in clinical applications. To our knowledge, this is the first demonstration of employing iron manganese silicates as pH-responsive T_1-T_2* dual-modal imaging contrast agents.

Fluorescence Imaging of FeMn(SiO_4) Hollow Nanospheres. The photoluminescence properties of FeMn(SiO_4) hollow nanospheres in PBS with pH 7.4 and pH 5 were investigated with the excitation wavelength of 514 nm. Figure 8a shows a yellow-green emission peak centered at 577 nm and red emission peaks centered at 624 and 684 nm. The multicolor emissions are aroused from the Mn^{2+} ions $^4E(^4G)-^6A_1(^6S)$ transition[42,43] because ^4G level of Mn atoms in the FeMn(SiO_4) lattice splits into four sublevels (Figure 8b): a 3-fold degenerate $^4T_1$ level, a 3-fold degenerate $^4T_2$ level, a 2-fold degenerate ^4E, and a non-degenerate $^4A_1$ level.[43] Furthermore, the intensity of the peaks centered at 624 and 684 nm in PBS with a pH of 5 are stronger than that in PBS with a pH of 7.4. Especially at the 684 nm, peak in PBS with pH = 5 is twice the intensity to that in PBS with pH = 7.4. As the concentration of hollow nanospheres in different PBS solutions is the same, the increase of the peak intensity can be attributed to the released Mn^{2+} ions in the acidic environment. According to the Sugano−Tanabe energy diagram (Figure 8c), the Mn^{2+} d−d transition is sensitive to the crystal field. And the electronic transition energy about ^4G, ^4D, ^4P, and ^4F to the ground state $^6A_{1g}$ (6S) of Mn^{2+} is strongly influenced by its coordination environment. Therefore, the d−d transition has a relationship with the crystal splitting parameter ΔE = 10 Dq.[44] Then, a model based on energy transfer mechanism (Figure 8d,e) has been suggested to further illustrate the above results. In a neutral solution, the majority of Mn^{2+} ions are localized at lattice sites of the crystal. The nonradiative energy transfer from the host to the $^4A_1$ (^4E) level of Mn^{2+} ions, followed by radiative energy transfer to the $^6A_1$ (6S) level of Mn^{2+} ions, leading to the green-yellow emission.[23] However, a large number of Mn^{2+} ions release in the acidic solution and occupy interstitial positions, making lattice defects where excitons can be trapped by the adjacent Mn^{2+} ions.[45] Because 3d valence electrons of Mn^{2+} ions are not protected by their surroundings and the ^4G level strongly depends on their surroundings, the d-d transitions are influenced.[23] Thus, Mn^{2+} ions close to lattice defects will be perturbed strongly, inducing their energy levels to shift to lower energies.[45] The increase of red fluorescence intensity is attributed to the emission from the $^4T_1$ (^4E)-$^6A_1$ (6S) transition of these perturbed Mn^{2+} ions. Generally, the released Mn^{2+} ions aroused by the low pH value of the acidic organelles can enhance the luminescence in the red band, inducing higher red-to-green ratio, which is beneficial for bioimaging. Though Mn^{2+} ions doped quantum dots or up conversion materials have been applied as fluorescence probes,[46,47] there are only a few reports about the application of single Mn^{2+} ions for bioimaging.

A549 human lung cancer cells treated with FeMn(SiO_4) hollow nanospheres were imaged under a confocal laser scanning microscopy (CLSM) to further study the in vitro bioimaging properties of the nanospheres. Green and red fluorescence (Figure 9b,c) are observed under the laser excitation with different wavelengths (488 and 543 nm). Combined with the luminescent results mentioned above, the generation of bright red fluorescence indicates that FeMn(SiO_4) hollow spheres are taken up by A549 cells and Mn^{2+} ions are released in the acidic organelles. The overlay of the bright field and fluorescent images (Figure 9d) verifies that the luminescence is originated from the intracellular region.

To verify that the red fluorescence from the cells was aroused by the released Mn^{2+} ions, the specific intracellular localization of FeMn(SiO_4) hollow nanospheres was tested by mcherry-LAMP-1 transfecting. Figure 9e−h shows that the green fluorescence from FeMn(SiO_4) hollow nanospheres and the red fluorescence from mcherry-LAMP-1 are overlapped, which indicates that the hollow spheres are localized in endosomes/lysosomes. As the nanoparticles with diameters ≤100 nm are usually taken up by cells via endocytosis,[48] we suggested that FeMn(SiO_4) hollow nanospheres entered into cells mainly through endocytosis. With the transportation from endosomes to lysosomes, the hollow nanospheres would locate in an acidic environment.[49] Then, Mn^{2+} ions could be released from FeMn(SiO_4) hollow nanospheres, enhancing the red fluorescence intensity.

Evaluation of Cytotoxicity. A549 cells were cultured with different concentrations of FeMn(SiO_4) hollow nanospheres for 24 h. Then, the cell viabilities against such nanospheres were investigated using MTT assay. The data (Figure 10) reveals that FeMn(SiO_4) hollow nanospheres cause no significant toxicity even at the concentration of 200 μg/mL, and the cell viability is approximately 80−90%. The cell viability

DOI: 10.1021/acsami.5b00727
ACS Appl. Mater. Interfaces 2015, 7, 5373−5383

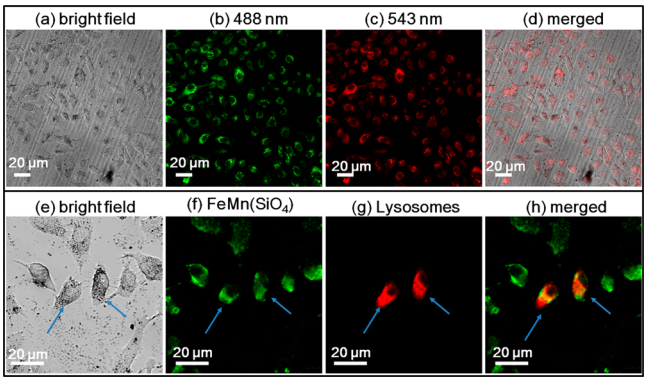

Figure 9. Confocal microscopy of (a) bright-field, fluorescent with excitation wavelengths of (b) 488 and (c) 543 nm, and (d) merged images for A549 cells after incubation with 50 μg/mL FeMn(SiO_4) hollow nanospheres for 24 h. (e–h) Subcellular localization of FeMn(SiO_4) hollow nanospheres observed by a confocal fluorescent microscopy. A549 cells transfected with mcherry-LAMP-1 were incubated with FeMn(SiO_4) hollow nanospheres for 24 h. (f) Fluorescence image of FeMn(SiO_4) hollow nanospheres. (g) Fluorescence image of mcherry-LAMP-1. (h) The overlap of the mcherry-LAMP-1 and FeMn(SiO_4) hollow nanospheres images indicates the colocalization of lysosomes and FeMn(SiO_4) hollow nanospheres. (In this experiment, we find that the luminous intensity of the nanospheres is weaker than that of mcherry-LAMP-1 with same intensity of excitation light. With the parameter of laser output set as 10%, the red fluorescence of mcherry-LAMP-1 can be observed obviously, while the red fluorescence of nanospheres is weak and almost invisible. Then, the parameter of laser output for FeMn(SiO_4) hollow nanospheres imaging was set as 15%. The parameter of laser output for mcherry-LAMP-1 imaging was set as 10%. Thus, the interference to the fluorescence image of mcherry-LAMP-1 induced by FeMn(SiO_4) hollow nanospheres could be eliminated through setting imaging parameters as mentioned above.).

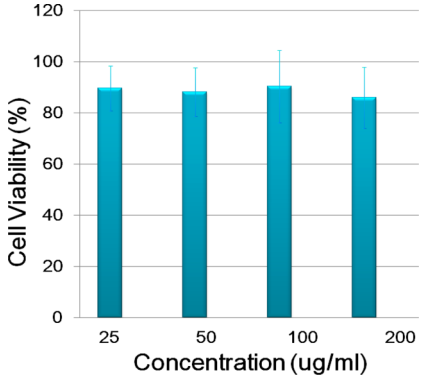

Figure 10. In vitro cytotoxicity of FeMn(SiO_4) hollow nanospheres at concentrations of 25, 50, 100, and 200 μg/mL.

value against FeMn(SiO_4) hollow nanospheres is a little lower than that against the traditional biocompatible silica nanoparticles.[50] As Mn^{2+} ions are known to be toxic, this result may be ascribed to the release of Mn^{2+} ions from FeMn(SiO_4) hollow nanospheres when they enter into the acidic organelles through endocytosis.[49] However, the pH-value of blood and normal tissues is about 7.4,[32] FeMn(SiO_4) hollow nanospheres in normal tissues should be stable. Because Mn elements are known to be essential in living organisms and they express toxicity only at high concentration (the adequate daily dietary intake amount of manganese for adults is 11 000 μg/day[51]), we therefore suggest that FeMn(SiO_4) hollow nanospheres are nontoxic to normal organisms and have satisfactory biocompatibility as bioimaging probes.

The Systematic Toxicity of FeMn(SiO_4) Hollow Nanospheres Formulation in Vivo. As FeMn(SiO_4) hollow nanospheres are finally concentrated in liver via RES, histological analysis of tissues was taken in healthy mice to further investigate the toxicity of the hollow nanospheres. FeMn(SiO_4) hollow nanospheres suspended in 200 μL of saline were injected into nude mice through the tail vein at a single dose of 60 mg/kg. Because a half-life of nanoparticles is about 25–30 h, the procedure of lymphatic transport and deposition often takes 24–36 h,[52] the mice were euthanized 36 h after contrast agents injection. The major organs, such as liver, kidneys, and lungs were surgically removed, followed by staining with hematoxylin and eosin (H&E). Figure 11 shows

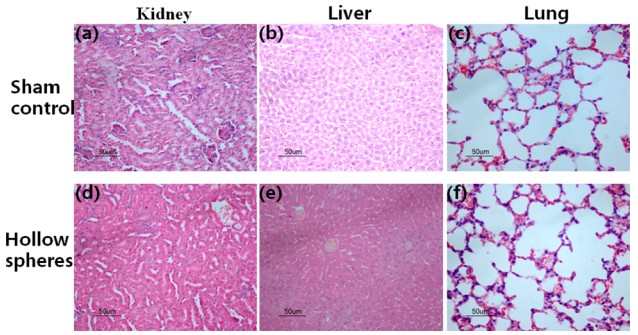

Figure 11. Histological analysis of three tissue organs (kidney, liver, lung) from mice after 36 h of (a–c) saline or (d–f) FeMn(SiO_4) hollow nanospheres intravenous injection, showing no changes in the cellular integrity or tissue morphology after the injection of FeMn(SiO_4) hollow nanospheres. The scale bar is 50 μm.

that all of the organs have well-organized cellular structure without obvious abnormality. MRI experiments in vivo have shown that FeMn(SiO_4) hollow spheres were mainly distributed in liver, no pathological changes in the liver section further confirms that the hollow nanospheres have low toxicity in vivo. FeMn(SiO_4) hollow spheres have good biocompatibility in vivo, indicated that they are promising pH-responsive T_1-T_2* dual-modal imaging contrast agents in the biomedical domain.

CONCLUSIONS

We have successfully synthesized a pH-responsive T_1-T_2* dual-modal contrast agent with auxiliary function of fluorescence imaging based on iron manganese silicate hollow nanospheres. Pretending to occupy the active sites in the olivine structure, Mn^{2+} ions can be released much easily from FeMn(SiO_4) hollow nanospheres by sensing the physiologically acidic environment. Cytotoxicity study and histology analysis showed excellent biocompatibility of these hollow nanospheres, which is necessary for their in vivo imaging application. MRI experiments in vivo showed that only 10 min after intravenous injection of the contrast agents, obvious distinction between the tumors and normal tissues can be observed easily through both T_1 and T_2* signals, with the assistance of their pH-responsive property. Though MR images for reticuloendothelial system (RES) organs demonstrated that the hollow nanospheres were mainly distributed in liver finally, the histology analysis showed that no pathophysiological changes could be observed from liver 36 h after intravenous administration of the nanospheres.

DOI: 10.1021/acsami.5b00727
ACS Appl. Mater. Interfaces 2015, 7, 5373–5383

Thus, $FeMn(SiO_4)$ hollow nanospheres without targeting agents grafted could be concentrated in tumors through EPR effect and serve as safe pH-responsive T_1-T_2* dual-modal contrast agents for different types of cancers imaging.

■ ASSOCIATED CONTENT

Supporting Information

EDS spectra of $FeMn(SiO_4)$ hollow nanospheres, N_2 adsorption and desorption isotherm and BJH poredistribution of the $FeMn(SiO_4)$ hollow nanospheres, $FeMn(SiO_4)$ olivine structure, hysteresis curves of the $FeMn(SiO_4)$ hollow nanospheres. This material is available free of charge via the Internet at http://pubs.acs.org.

■ AUTHOR INFORMATION

Corresponding Authors

*E-mail: cqw@ustc.edu.cn. Fax: +86-551-63603005.
*E-mail: zhenguo@ustc.edu.cn.
*E-mail: whblqh@mail.ustc.edu.cn.

Notes

The authors declare no competing financial interest.

■ ACKNOWLEDGMENTS

We thank Dr. Xuannv Zhao for LAMP-1 plasmids. This work was supported by the National Natural Science Foundation of China, 21271163, U1232211 (Q.-W.C.), 31100992 (Z.G.), the Program for Changjiang Scholars and MOE Innovative Research Team IRT13038 (Z.G.), and the Ph.D. Program of the Foundation of Ministry of Education of China 20113402120041 (Z. Guo).

■ REFERENCES

(1) Huang, Y.; Hu, L.; Zhang, T.; Zhong, H.; Zhou, J.; Liu, Z.; Chen, Q. Mn_3 $[Co(CN)_6]_2$@SiO_2 Core-Shell Nanocubes: Novel Bimodal Contrast Agents for MRI and Optical Imaging. *Sci. Rep.* **2013**, *3*, 1−7.

(2) Hou, Y.; Qiao, R.; Fang, F.; Wang, X.; Dong, C.; Liu, K.; Liu, C.; Liu, Z.; Lei, H.; Wang, F.; Gao, M. $NaGdF_4$ Nanoparticle-Based Molecular Probes for Magnetic ResonanceImaging of Intraperitoneal Tumor Xenografts in Vivo. *ACS Nano* **2013**, *7*, 330−338.

(3) Chen, Y.; Li, M.; Hong, Y.; Lam, J. W.; Zheng, Q.; Tang, B. Z. Dual-Modal MRI Contrast Agent with Aggregation-Induced Emission Characteristic for Liver Specific Imaging with Long Circulation Lifetime. *ACS Appl. Mater. Interfaces* **2014**, *6*, 10783−10791.

(4) Peter, C.; Jeffrey, J. E.; Thomas, J. M.; Randall, B. L. Gadolinium(III) Chelates as MRI Contrast Agents: Structure, Dynamics, and Applications. *Chem. Rev.* **1999**, *99*, 2293−2352.

(5) Na, H. B.; Song, I. C.; Hyeon, T. Inorganic Nanoparticles for MRI Contrast Agents. *Adv. Mater.* **2009**, *21*, 2133−2148.

(6) Na, H. B.; Lee, J. H.; An, K.; Park, Y. I.; Park, M.; Lee, I. S.; Nam, D. H.; Kim, S. T.; Kim, S. H.; Kim, S. W.; Lim, K. H.; Kim, K. S.; Kim, S. O.; Hyeon, T. Development of a T_1 Contrast Agent for Magnetic Resonance Imaging Using MnO Nanoparticles. *Angew. Chem., Int. Ed.* **2007**, *46*, 5397−5401.

(7) Seo, W. S.; Lee, J. H.; Sun, X.; Suzuki, Y.; Mann, D.; Liu, Z.; Dai, H. FeCo/Graphitic-Shell Nanocrystals as Advanced Magnetic-Resonance-Imaging and Near-Infrared Agents. *Nat. Mater.* **2006**, *5*, 971−976.

(8) Yang, H.; Zhuang, Y.; Sun, Y.; Dai, A.; Shi, X.; Wu, D.; Li, F.; Hu, H.; Yang, S. Targeted Dual-Contrast T_1- and T_2-Weighted Magnetic Resonance Imaging of Tumors Using Multifunctional Gadolinium-Labeled Superparamagnetic Iron Oxide Nanoparticles. *Biomaterials* **2011**, *32*, 4584−4593.

(9) Zhou, Z.; Huang, D.; Bao, J.; Chen, Q.; Liu, G.; Chen, Z.; Chen, X.; Gao, J. A Synergistically Enhanced T_1-T_2 Dual-Modal Contrast Agent. *Adv. Mater.* **2012**, *24*, 6223−6228.

(10) Allen, T. M.; Cullis, P. R. Drug Delivery Systems: Entering the Mainstream. *Science* **2004**, *303*, 1818−1822.

(11) Brannon-Peppas, L.; Blanchette, J. O. Nanoparticle and Targeted Systems for Cancer Therapy. *Adv. Drug Delivery Rev.* **2012**, *64*, 206−212.

(12) Xiong, L. Q.; Chen, Z. G.; Yu, M. X.; Li, F. Y.; Liu, C.; Huang, C. H. Synthesis, Characterization, and in Vivo Targeted Imaging of Amine-Functionalized Rare-Earth up-Converting Nanophosphors. *Biomaterials* **2009**, *30*, 5592−5600.

(13) Huang, G.; Si, Z.; Yang, S.; Li, C.; Xing, D. Dextran-based pH-Sensitive Near-Infrared Nanoprobe for in Vivo Differential-Absorption Dual-Wavelength Photoacoustic Imaging of Tumors. *J. Mater. Chem.* **2012**, *22*, 22575−22581.

(14) Lee, E. S.; Gao, Z.; Bae, Y. H. Recent Progress in Tumor pH Targeting Nanotechnology. *J. Controlled Release* **2008**, *132*, 164−170.

(15) Bennewitz, M. F.; Lobo, T. L.; Nkansah, M. K.; Ulas, G.; Brudvig, G. W.; Shapiro, E. M. Biocompatible and pH-Sensitive PLGA Encapsulated MnO Nanocrystals for Molecular and Cellular MRI. *ACS Nano* **2011**, *5*, 3438−3446.

(16) Kim, S. M.; Im, G. H.; Lee, D. G.; Lee, J. H.; Lee, W. J.; Lee, I. S. Mn^{2+}-Doped Silica Nanoparticles for Hepatocyte-Targeted Detection of Liver Cancer in T_1-Weighted MRI. *Biomaterials* **2013**, *34*, 8941−8948.

(17) Kim, T.; Cho, E. J.; Chae, Y.; Kim, M.; Oh, A.; Jin, J.; Lee, E. S.; Baik, H.; Haam, S.; Suh, J. S.; Huh, Y. M.; Lee, K. Urchin-Shaped Manganese Oxide Nanoparticles as pH-Responsive Activatable T_1 Contrast Agents for Magnetic Resonance Imaging. *Angew. Chem., Int. Ed.* **2011**, *123*, 10777−10781.

(18) Hutchison, J. E. Greener Nanoscience: A Proactive Approach to Advancing Applications and Reducing Implications of Nanotechnology. *ACS Nano* **2008**, *2*, 395−402.

(19) Lin, K.; Zhai, W.; Ni, S.; Chang, J.; Zeng, Y.; Qian, W. Study of the Mechanical Property and in Vitro Biocompatibility of $CaSiO_3$ Ceramics. *Ceram. Int.* **2005**, *31*, 323−326.

(20) Yang, H.; Shi, J.; Gong, M. A Novel Approach for Preparation of Zn_2SiO_4:Tb Nanoparticles by Sol−Gel-Microwave Heating. *J. Mater. Sci.* **2005**, *40*, 6007−01010.

(21) Redfern, S. A.; Henderson, C. M. B.; Knight, K. S.; Wood, B. J. High-Temperature Order−Disorder in $(Fe_{0.5}Mn_{0.5})_2SiO_4$ and $(Mg_{0.5}Mn_{0.5})_2SiO_4$ Olivines; A in Situ Neutron Diffraction Study. *Eur. J. Mineral.* **1997**, *9*, 287−300.

(22) Kirfel, A.; Lippmann, T.; Blaha, P.; Schwarz, K.; Cox, D. F.; Rosso, K. M.; Gibbs, G. V. Electron Density Distribution and Bond Critical Point Properties for Forsterite, Mg_2SiO_4, Determined with Synchrotron Single Crystal X-ray Diffraction Data. *Phys. Chem. Miner.* **2005**, *32*, 301−313.

(23) Herrmann, A.; Ehrt, D. Time Resolved Fluorescence Measurements on Tb^{3+} and Mn^{2+} Doped Glasses. *Glass Sci. Technol.* **2005**, *78*, 99−105.

(24) Stöber, W.; Fink, A.; Bohn, E. Controlled Growth of Monodisperse Silica Spheres in the Micron Size Range. *J. Colloid Interface Sci.* **1968**, *26*, 62−69.

(25) Wang, Y.; Wang, G.; Wang, H.; Liang, C.; Cai, W.; Zhang, L. Chemical-Template Synthesis of Micro/Nanoscale Magnesium Silicate Hollow Spheres for Waste-Water Treatment. *Chem.—Eur. J.* **2010**, *16*, 3497−3503.

(26) Palmer, D. A.; Drummond, S. E. Thermal Decarboxylation of Acetate. Part I. The Kinetics and Mechanism of Reaction in Aqueous Solution. *Geochim. Cosmochim. Acta* **1986**, *50*, 813−823.

(27) Iler, R. K. The Colloid Chemistry of Silica and Silicates. *Soil Sci.* **1955**, *80*, 86.

(28) Fang, Q.; Xuan, S.; Jiang, W.; Gong, X. Yolk-like Micro/Nanoparticles with Superparamagnetic Iron Oxide Cores and Hierarchical Nickel Silicate Shells. *Adv. Funct. Mater.* **2011**, *21*, 1902−1909.

(29) HnzrNr, R. M. Effects of Temperature and Pressure on the Crystal Structure of Ferromagnesian Olivine. *Am. Mineral.* **1977**, *62*, 286−295.

DOI: 10.1021/acsami.5b00727
ACS Appl. Mater. Interfaces 2015, 7, 5373−5383

(30) Burton, A.; Accardi, R. J.; Lobo, R. F.; Falcioni, M.; Deem, M. W. MCM-47: A Highly Crystalline Silicate Composed of Hydrogen-Bonded Ferrierite Layers. *Chem. Mater.* **2000**, *12*, 2936−2942.
(31) Barbe, C.; Bartlett, J.; Kong, L.; Finnie, K.; Lin, H. Q.; Larkin, M.; Calleja, S.; Bush, A.; Calleja, G. Silica Particles: A Novel Drug-Delivery System. *Adv. Mater.* **2004**, *16*, 1959−1966.
(32) Yuan, Y.; Ding, D.; Li, K.; Liu, J.; Liu, B. Tumor-Responsive Fluorescent Light-up Probe Based on a Gold Nanoparticle/Conjugated Polyelectrolyte Hybrid. *Small* **2014**, *10*, 1967−1975.
(33) Bragg, W. L.; Brown, G. B. XXX. Die Struktur des Olivins. *Z. Kristallogr.* **1926**, *63*, 538−552.
(34) Lartigue, L.; Hugounenq, P.; Alloyeau, D.; Clarke, S. P.; Lévy, M.; Bacri, J. C.; Bazzi, R.; Brougham, D. F.; Wilhelm, C.; Gazeau, F. Cooperative Organization in Iron Oxide Multi-Core Nanoparticles Potentiates Their Efficiency as Heating Mediators and MRI Contrast Agents. *ACS Nano* **2012**, *6*, 10935−10949.
(35) Hadjipanayis, C. G.; Bonder, M. J.; Balakrishnan, S.; Wang, X.; Mao, H.; Hadjipanayis, G. C. Metallic Iron Nanoparticles for MRI Contrast Enhancement and Local Hyperthermia. *Small* **2008**, *4*, 1925−1929.
(36) Choi, J. S.; Lee, J. H.; Shin, T. H.; Song, H. T.; Kim, E. Y.; Cheon, J. Self-Confirming "AND" Logic Nanoparticles for Fault-Free MRI. *J. Am. Chem. Soc.* **2010**, *132*, 11015−11017.
(37) Gao, J.; Zhang, B.; Gao, Y.; Pan, Y.; Zhang, X.; Xu, B. Fluorescent Magnetic Nanocrystals by Sequential Addition of Reagents in a One-Pot Reaction: A Simple Preparation for Multifunctional Nanostructures. *J. Am. Chem. Soc.* **2007**, *129*, 11928−11935.
(38) Shin, J.; Anisur, R. M.; Ko, M. K.; Im, G. H.; Lee, J. H.; Lee, I. S. Hollow Manganese Oxide Nanoparticles as Multifunctional Agents for Magnetic Resonance Imaging and Drug Delivery. *Angew. Chem., Int. Ed.* **2009**, *48*, 321−324.
(39) Arbab, A. S.; Wilson, L. B.; Ashari, P.; Jordan, E. K.; Lewis, B. K.; Frank, J. A. A Model of Lysosomal Metabolism of Dextran Coated Superparamagnetic Iron Oxide (SPIO) Nanoparticles: Implications for Cellular Magnetic Resonance Imaging. *NMR Biomed.* **2005**, *18*, 383−389.
(40) Hu, T. C.; Chuang, K. H.; Yanasak, N.; Koretsky, A. P.Improved Cardiac Manganese-Enhanced MRI (MEMRI) with T_1 Mapping in Rodent. In Proceedings of the IEEE 33rd Annual Northeast Bioengineering Conference, 2007. Long Island, NY, March 10−11, 2007, 73−74.
(41) Albanese, A.; Tang, P. S.; Chan, W. C. The Effect of Nanoparticle Size, Shape, and Surface Chemistry on Biological Systems. *Annu. Rev. Biomed. Eng.* **2012**, *14*, 1−16.
(42) Geng, B. Y.; Zhang, L. D.; Wang, G. Z.; Xie, T.; Zhang, Y. G.; Meng, G. W. Synthesis and Photoluminescence Properties of ZnMnS Nanobelts. *Appl. Phys. Lett.* **2004**, *84*, 2157−2159.
(43) Sirkeli, V. P.; Nedeoglo, D. D.; Nedeoglo, N. D.; Radevici, I. V.; Sobolevskaia, R. L.; Sushkevich, K. D.; Hartnagel, H. L. Magnetic and Luminescent Properties of Manganese-Doped ZnSe Crystals. *Phys. B* **2012**, *407*, 3802−3807.
(44) Ye, R.; Jia, G.; Deng, D.; Hua, Y.; Cui, Z.; Zhao, S.; Huang, L.; Wang, H.; Li, C.; Xu, S. Controllable Synthesis and Tunable Colors of α- and β-Zn_2SiO_4: Mn^{2+} Nanocrystals for UV and Blue Chip Excited White LEDs. *J. Phys. Chem. C* **2011**, *115*, 10851−10858.
(45) Powell, R. C.; Elouadi, B.; Xi, L.; Loiacono, G. M.; Feigelson, R. S. Optical Spectroscopy of Mn_2SiO_4 Crystals. *J. Phys. Chem.* **1986**, *84*, 657−661.
(46) Geszke-Moritz, M.; Piotrowska, H.; Murias, M.; Balan, L.; Moritz, M.; Lulek, J.; Schneider, R. Thioglycerol-Capped Mn-Doped ZnS Quantum Dot Bioconjugates as Efficient Two-Photon Fluorescent Nano-Probes for Bioimaging. *J. Mater. Chem. B* **2013**, *1*, 698−706.
(47) Zeng, S.; Yi, Z.; Lu, W.; Qian, C.; Wang, H.; Rao, L.; Zeng, T.; Liu, H.; Liu, H.; Fei, B. Simultaneous Realization of Phase/Size Manipulation, Upconversion Luminescence Enhancement, and Blood Vessel Imaging in Multifunctional Nanoprobes Through Transition Metal Mn^{2+} Doping. *Adv. Funct. Mater.* **2014**, *24*, 4051−4059.
(48) Osaki, F.; Kanamori, T.; Sando, S.; Sera, T.; Aoyama, Y. A Quantum Dot Conjugated Sugar Ball and Its Cellular Uptake. On the Size Effects of Endocytosis in the Subviral Region. *J. Am. Chem. Soc.* **2004**, *126*, 6520−6521.
(49) Conner, S. D.; Schmid, S. L. Regulated Portals of Entry into the Cell. *Nature* **2003**, *422*, 37−44.
(50) Chen, Y.; Chen, H.; Ma, M.; Chen, F.; Guo, L.; Zhang, L.; Shi, J. Double Mesoporous Silica Shelled Spherical/Ellipsoidal Nanostructures: Synthesis and Hydrophilic/Hydrophobic Anticancer Drug Delivery. *J. Mater. Chem.* **2011**, *21*, 5290−5298.
(51) Annan, K.; Kojo, A. I.; Cindy, A.; Samuel, A. N.; Tunkumgnen, B. M. Profile of Heavy Metals in Some Medicinal Plants from Ghana Commonly Used as Components of Herbal Formulations. *Pharmacogn. Res.* **2010**, *2*, 41.
(52) Feldman, A. S.; McDougal, W. S.; Harisinghani, M. G. The Potential of Nanoparticle-Enhanced Imaging. *Urol. Oncol.: Semin. Orig. Invest.* **2008**, *26*, 65−73.
(53) Blasse, G.; Grabmaier, B. C. *Luminescent Materials*; Springer: Berlin, 1994.

DOI: 10.1021/acsami.5b00727
ACS Appl. Mater. Interfaces 2015, 7, 5373−5383